Proceedings of FEDSM2006
2006 ASME Joint U.S. - European Fluids Engineering Summer Meeting
July 17-22, 2006, Miami, FL

FEDSM2006-98553
Keynote Lecture

THREE-DIMENSIONAL PLASMA-BASED STALL CONTROL SIMULATIONS WITH COUPLED FIRST-PRINCIPLES APPROACHES

Datta V. Gaitonde[*] **& Miguel R. Visbal**
Computational Sciences Branch
Air Vehicles Directorate
Air Force Research Laboratory
Wright-Patterson AFB, OH 45433
Email: Datta.Gaitonde@wpafb.af.mil

Subrata Roy
Computational Plasma Dynamics Laboratory
Mechanical Engineering Department
Kettering University
Flint, Michigan
Email: sroy@kettering.edu

ABSTRACT

Numerical simulations are employed to understand the mechanisms by which asymmetric dielectric barrier discharges operating at radio frequencies reduce or eliminate stall. The specific focus is on a NACA 0015 wing section at a nominal Reynolds number of $45,000$ and 15 degree angle-of-attack. The body force is obtained separately from both phenomenological and first-principles based models. To overcome the daunting complexity of the latter approach, a procedure to couple unsteady force fields obtained from multi-fluid models to very high-fidelity implicit large-eddy simulations is developed, implemented and evaluated for a $5kHz$ signal. The paper discusses results with both approaches to understand the effect of Reynolds number, angle of attack, actuator strength and location as well as unsteadiness of actuation through radio frequency excitation and duty cycle variation. The results are assimilated in the context of the combined impact of near wall momentum enhancement and transition to turbulence. It is shown that force fluctuations at radio-frequencies result in the development of a rich turbulence structure downstream of actuation. These observations, as well as details of the acoustic signal, cannot be obtained from the simplified steady force model. For higher Reynolds numbers and relatively lower actuation forces, mechanisms that enhance turbulence development are the dominant consideration. These include not only radio-frequency force variations, but also streamwise vorticity generation through edge effects associated with finite-span actuation and wide-spectrum input associated with switch-on/switch-off inherent in duty cycles.

1 INTRODUCTION

Plasma-based techniques of flow control have numerous advantages over more conventional approaches. Particularly attractive is the absence of moving parts and mass injection (and thus mechanical inertia), rapid on-off capability and access to high frequencies and large forces and energy associated with electromagnetic fields. Although various configurations are being explored at both high and low speeds, the most striking experimental evidence has revealed greatest effectiveness in the latter regime at atmospheric pressures. Unit devices employed for this purpose typically consist of one electrode exposed to the flow (and generally flush with the surface) and another embedded downstream in the dielectric, as shown in Fig. 1. A radio-frequency signal (*e.g.*, 2 kV, 5 kHz) is applied to the exposed electrode, while the embedded electrode is grounded. Under these conditions, a complex sequence of events occurs, key among which is ionization of the near wall air, causing a localized discharge. Visualizations (*e.g.* have demonstrated that the actuator can then eliminate stall (*e.g.*, Refs. [1–7]). However, details of the mechanism by

---

[*] Address all correspondence to this author

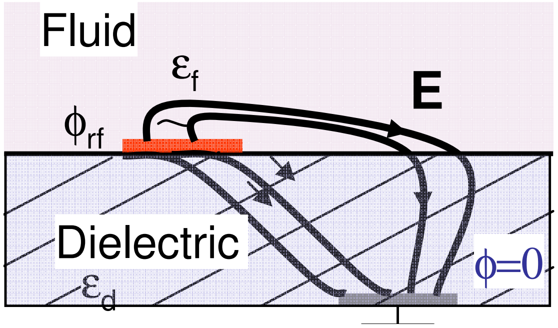

Figure 1. SCHEMATIC OF ACTUATOR

which this effect is accomplished remain relatively unknown. Several papers have postulated phenomenologies of varying complexity. For example, Ref. [8] correlates the body force to an electric pressure gradient while Ref. [9] draws a connection to a Lorentz force through development of a charged region subjected to an electric field. Momentum coupling including compressibility effects have also been proposed [10].

Recently, the model of Shyy *et al* [9] was employed to examine the effect of body force on several fluid dynamic problems, including flows past flat plates, airfoils and delta wings [11–13]. Numerous conclusions were derived from steady and transient (duty-cycle) force fields. Two main mechanisms were identified: enhancement of near-wall momentum and triggering of transition to turbulence. While the former effect may be computed with 2-D configurations, the latter requires full 3-D treatment through direct numerical simulations (DNS) and Large-Eddy Simulations (LES) since spanwise instabilities and their development are a key feature of such flowfields. In this paper therefore, all simulations described are performed in 3-D, with the Navier-Stokes equations supplemented with body force terms as described in § 2. The baseline stalled flow field is described in § 3. Some of the main conclusions derived from numerous exploratory studies with a phenomenological model are summarized in the context of the airfoil flow problem in § 4.

The motivation to replace the steady force model with a more sophisticated approach, which tracks the variation of force in each cycle of the time-varying signal, stems not only from the need for higher fidelity, but also from the fact that the effect on turbulence appears dominated by the unsteadiness of the force due to the duty cycle [12]. A fully first-principles approach is not currently feasible however because plasma collision phenomena occur on a time scale that is several orders of magnitude smaller than that of the fluid inertial and viscous scales or even the time scale associated with the excitation signal. To make this broad-spectrum problem amenable to high-fidelity solutions, a coupled approach is required in which the fundamental plasma processes associated with charged particles (§ 5.1) are solved separately to yield the instantaneous charge and electric field. The time-varying force is then coupled to the Navier-Stokes equations as described in § 5.2. This procedure involves several assumptions, and requires care because of the wide disparity in sizes of the mesh on which force is computed and that on which its effect on the fluid dynamics is determined. Finally, in § 5.3, several pioneering fully 3-D coupled simulations demonstrating stall control are presented and discussed in the context of unsteady and time-averaged responses.

2 THEORETICAL MODEL

The strong conservation form of the full 3-D Navier-Stokes equations are solved in general curvilinear coordinates with body force terms. The general form the equations may be written as:

$$\frac{\partial \hat{X}}{\partial t}+\frac{\partial \hat{F}_I}{\partial \xi}+\frac{\partial \hat{G}_I}{\partial \eta}+\frac{\partial \hat{H}_I}{\partial \zeta}=\frac{\partial \hat{F}_V}{\partial \xi}+\frac{\partial \hat{G}_V}{\partial \eta}+\frac{\partial \hat{H}_V}{\partial \zeta}+\hat{S} \qquad (1)$$

where, $\hat{X}=\{\rho,\ \rho u,\ \rho v,\ \rho w,\ \rho e\}/J$ is the solution vector, J is the transformation Jacobian and $\hat{F}$, $\hat{G}$ and $\hat{H}$ are the flux vectors (subscripts I and V refer to inviscid and viscous components respectively). All quantities are non-dimensionalized with reference values, length $L_{ref}=c$ (chord), velocity $U_{ref}=U_\infty$, density $\rho_{ref}=\rho_\infty$ and temperature T_∞. Details of the individual flux vectors may be found in Ref. [13]. For subsequent reference, the source term is:

$$\hat{S}=\frac{1}{J}\left\{\begin{array}{c} 0 \\ D_c\rho_c e_c E_x \\ D_c\rho_c e_c E_y \\ D_c\rho_c e_c E_z \\ D_c\beta\rho_c(uE_x+vE_y+wE_z) \end{array}\right\} \qquad (2)$$

e_c is the electronic charge and the parameter D_c represents the scaling of the electrical to inertial forces:

$$D_c=\frac{\rho_{c,ref}\,e_c E_{ref} L_{ref}}{\rho_{ref} U_{ref}^2} \qquad (3)$$

Details of the charge number density, ρ_c and electric field vector $\vec{E}=\{E_x,E_y,E_z\}$ are derived from either phenomenological and first-principles components. Both approaches are described below in due course.

All wing-section simulations are performed at a very low Mach number of 0.1. The nominal Reynolds number is $45,000$ and the angle-of-attack is 15^o: the effect of varying these parameters is outlined in § 4.4. The spanwise

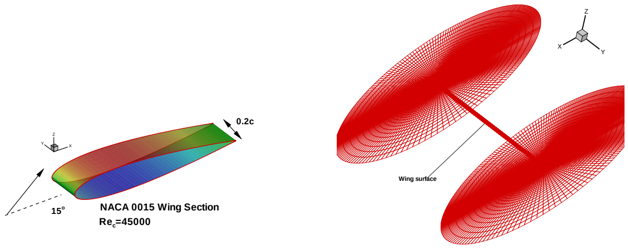

(a) Problem simulated (b) Overview of grid structure

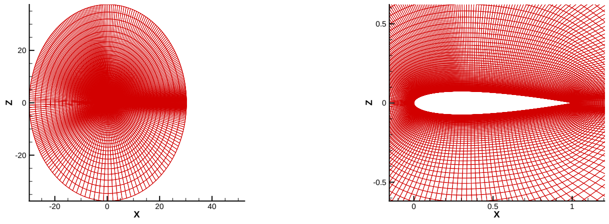

(c) Sectional view (d) Enlarged view

Figure 2. GRID STRUCTURE

extent of the domain is taken to be $0.2c$, where c is the chord length. An O-type mesh is employed, comprised of $308 \times 75 \times 145$ points in the x (streamwise), y (spanwise) and z (body-normal) directions respectively. The grid is generated by stacking planes in the manner shown in Fig. 2b. A view of each section is shown in Fig.2c, with an enlarged view in Fig. 2d. The mesh is stretched rapidly in the far-field towards the outer boundary, which is located $30c$ from the surface of the airfoil. No-slip, zero body-normal pressure-gradient and isothermal wall conditions are enforced at the solid-wall. The far field is assumed to be far enough away for free-stream conditions to be valid while periodic conditions are applied in the spanwise direction as well as at the branch cut arising due to the O-type mesh.

A high-order compact-difference method discretizes the governing equations. Derivatives, ϕ', of each required quantity, ϕ, are obtained in the uniform transformed plane (ξ, η, ζ) with the formula:

$$\Gamma_s \phi'_{i-1} + \phi'_i + \Gamma_s \phi'_{i+1} = b_s \frac{\phi_{i+2} - \phi_{i-2}}{4} + a_s \frac{\phi_{i+1} - \phi_{i-1}}{2} \quad (4)$$

where Γ_s, a_s and b_s determine the spatial properties of the scheme. All simulations described in this work employ the sixth-order *C6* method, for which $\Gamma_s = 1/3$, $a_s = 14/9$ and $b_s = 1/9$. Details of the spectral characteristics of these schemes, and others obtainable from Eqn. 4, may be found in Refs. [14, 15].

Additional components are required in the method to enforce numerical stability, which can be compromised by mesh stretching, boundary condition implementation and non-linear phenomena. Spurious frequencies in the solution are systematically removed with a filter designed using spectral analysis. For any component of the conserved vector, ϕ:

$$\alpha_f \hat{\phi}_{i-1} + \hat{\phi}_i + \alpha_f \hat{\phi}_{i+1} = \Sigma_{n=0}^{N} \frac{a_n}{2} (\phi_{i+n} + \phi_{i-n}) \quad (5)$$

where $\hat{\phi}$ is the filtered value. Relevant spectral analyses may be found in Ref. [16]. For these simulations, the $8th$-order filter with $\alpha_f = 0.2$ is employed in the body-normal and streamwise directions, while the $10th$ order filter with $\alpha_f = 0.4$ is chosen in the spanwise periodic direction.

3 BASELINE FLOW

The nominal flow is shown in Fig. 3, with iso-levels of instantaneous vorticity magnitude colored by the spanwise component of vorticity (Fig. 3a) and instantaneous (3b) and mean (3c) velocity contours in the mid-span plane. A shear layer emanates from the separation point, which occurs at approximately 2% chord and the flow may be considered to be fully stalled. Proceeding downstream, the layer loses its coherence as the three-dimensional break-up process progresses. The flow beneath the shear layer is transitional, and is characterized by very low velocities. It has been shown in Ref. [11], that the absence of a spanwise breakdown mechanism in a 2-D computation at the same flow parameters yields a vastly different pattern in both instantaneous and mean features. Vortices maintain their form in an unphysical fashion, resulting in a sequence of large vortex pairs that are shed downstream at various intervals. Peak instantaneous velocities are considerably larger, reaching almost twice those observed in the 3-D simulations. In a consistent fashion, instantaneous pressure contours exhibit coherent features in which extrema are much higher than in the full simulation. Further details of the no-control flow may be found in Ref. [11]. Some pertinent aspects will be reiterated below in the context of new results where warranted.

4 RESULTS WITH PHENOMENOLOGICAL MODEL

An overview is first presented of some broad features of the response of the stalled airfoil flow to the phenomenological force model of Shyy *et al.*

4.1 SIMPLIFIED FORCE FIELD MODEL

In this simplified model, the body force is assumed to be steady, with the implicit assumption that the fluid response is independent of variations within each excitation cycle. The force is obtained from

$$\vec{F} = D_c \theta \Delta t \alpha \rho_c \vec{E} \delta \quad (6)$$

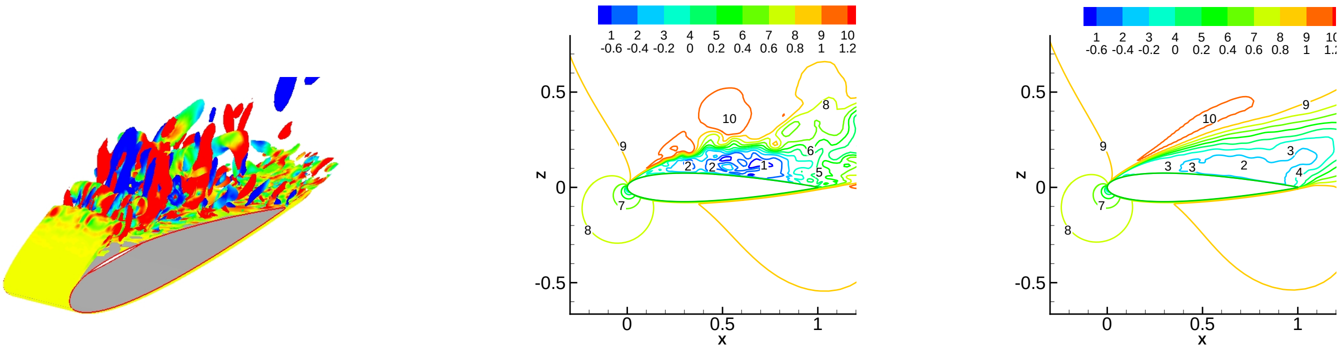

(a) 3-D structure - iso-levels of vorticity (b) instantaneous u-velocity (mid-span) (c) mean u-velocity

Figure 3. STRUCTURE OF 3-D FLOWFIELD WITHOUT CONTROL

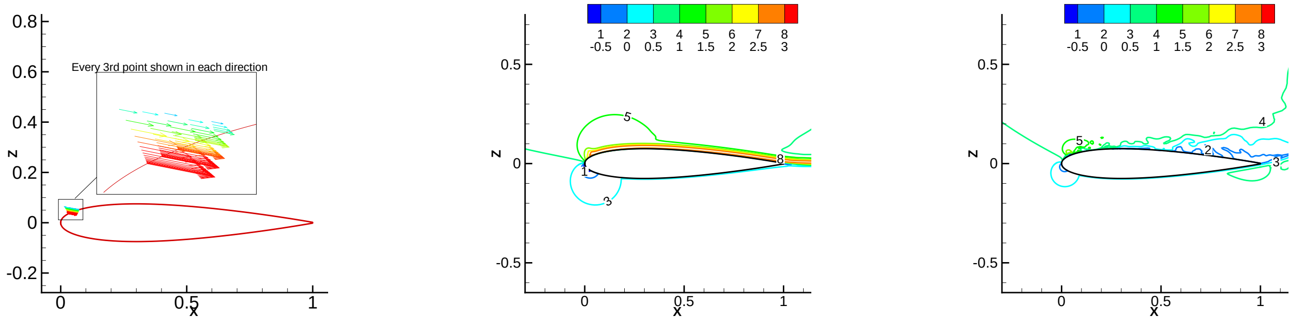

(a) Force field (b) Downstream oriented force (c) Force towards body

Figure 4. STEADY FORCE AND EFFECT ON u-VELOCITY WITH PHENOMENOLOGICAL MODEL

where θ is the frequency of the applied voltage, Δt is an effective intra-cycle duty cycle to recover a mean force, α is a factor for collision efficiency, ρ_c is the charge density, $\vec{E}$ is the electric field vector and δ constrains the region of force. The charge density is assumed to be uniform in the region of interest. The variation in electric field is approximated through several assumptions. The magnitude is assumed to vary linearly in x and z measured from the downstream edge of the exposed electrode, $|E| = E_o - k_1 x - k_2 z$. The peak value ($E_o = V/d$, where V is the applied voltage and d is the streamwise distance between the two electrodes) occurs near the origin. A further assumption is made that the field value is at or above breakdown level (E_b) in the plasma region, so that $\delta = 1$ when $|E| > E_b$ and $\delta = 0$ otherwise. By choosing the streamwise and body normal extents (b_d and a_d respectively), the values of $k_1 = (E_o - E_b)/b_d$ and $k_2 = (E_o - E_b)/a_d$ are determined. In the frame of reference of the device, $\vec{E}$ is then obtained from:

$$\vec{E} = \frac{|E|}{\sqrt{k_1^2 + k_2^2}} \left\{ \kappa_\xi k_2 \hat{\xi} + \kappa_\eta k_1 \hat{\eta} \right\} \qquad (7)$$

Here, $\hat{\xi}$ and $\hat{\eta}$ are unit vectors aligned respectively along and normal to the exposed electrode, which is assumed to lie flush on the surface of the body. For the wing, this coordinate system is located at the tangent to the surface at the leading edge of the electrode. In all cases, a single actuator is assumed, though its location and strength are varied. The body force orientation is adjusted by choosing κ_ξ and κ_η to yield variants of the Shyy model as described in Ref. [11]. The values of $\theta = 3000$, $\Delta t = 67\mu s$, $\alpha = 1$, $\rho_c = 10^{11}/cm^3$ are taken from Ref. [9]. The nominal values chosen for the parameters describing strength and extent are $D_c = 2400$, $a_d = 0.018$ are $b_d = 0.024$, where a and b are normalized by chord length. Effects of D_c variation are described in § 4.5 and § 5.3 for the phenomenological and first-princples-derived force fields respectively. For the former approach described in this section, the body force obtained when the actuator is placed near the leading edge with origin at $X_o = 0.028$, $Z_o = 0.034$, is shown in Fig.4a at the mid-span location. Note that unless otherwise mentioned, the force has no gradients in the spanwise direction.

4.2 STEADY FORCE IN DIRECTION OF FLOW

Results with two variants of the Shyy model, corresponding to $\kappa_\xi = 1$ and $\kappa_\eta = -1$, in which the force has significant streamwise and downward components, and $\kappa_\xi = 0$ and $\kappa_\eta = -1$, in which vertical force component points towards the surface are shown in Fig. 4b and c respectively. The *u*-velocity contours indicate that separation is substantially eliminated in both cases. In the former, the flow becomes nearly steady, but modest low frequency oscillations are observed in the wake downstream of the trailing edge. In this region, the mesh is relatively coarse, and potential instabilities in the wake may be constrained by the finiteness of the spanwise extent of the domain. Force orientations that are predominantly towards the surface (Fig. 4c) reduce the size of the disturbed region but the solution remains unsteady as coherent structures are triggered and then convected downstream.

Steady force calculations were also employed to examine the impact of the work term in the energy equation *i.e.,* $D_c q^* \vec{U} \cdot \vec{E}^*$. The results (not shown, see Ref. [11]) indicate that there are no noteworthy quantitative differences for this low speed flow.

4.3 DUTY CYCLE EFFECTS

Impulses associated with startup and shutdown can be incorporated into duty cycles, in which the actuator is switched on and off intermittently in a usually regular pattern. Duty cycles can enhance effectiveness by reducing the power requirement [17]. However, the results of Ref. [12] demonstrate that duty cycles also have a very profound impact on the flow when the turbulence mechanism is activated. A brief illustration is now provided in the context of the wing section.

A key parameter in the imposition of the duty cycle is the interpulse period. As a starting point, a reasonable choice may be made by examining the evolution of an attached flow after cessation of the body force. Results described in Ref. [11] indicate that when a steady actuator is suddenly switched off, the wall jet gradually ceases to exist and discernable leading edge separation, expected at 15^o angle-of-attack occurs after about $0.7T_c$, where $T_c = c/U_\infty$ is the characteristic time. This unsteady separation phenomenon is characterized by the onset of reversed flow and formation of vortices similar to those observed in the initiation of dynamic stall. The first inter-pulse period explored is thus fixed at $0.7T_c$. The amplitude of the imposed force is shown in Fig. 5 as a function of time. With duty cycle of 20%, the actuator is on for $0.14T_c$ in each cycle. Details of the equation employed to generate the profile are provided in Ref. [13].

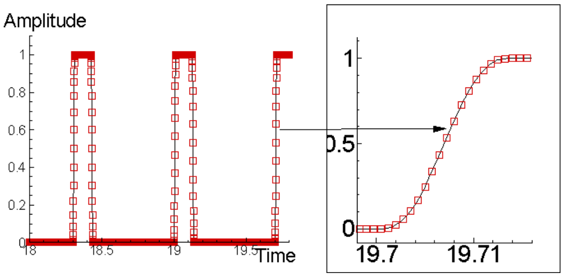

Figure 5. AMPLITUDE VARIATION IN DUTY CYCLE, $T_p = 0.7T_c$

The response may be naturally divided into two time ranges: the initial transients and the asymptotic state. For the former, the actuator operates in an environment dominated by the initial condition shown earlier in Fig. 3, in which a clear separated flow is observed with a shear layer that rapidly becomes turbulent. Details of this transient process may be found in Ref. [13].

After several characteristic times, an asymptotic state is reached, which is described in Fig. 6. Figure 6a depicts the situation at roughly the mid-point of the off segment of the cycle. A major feature in each figure is the existence of relatively large convecting coherent structures outside of the near wall region. This is observed to be the direct result of the impulsive nature of the forcing. Upon switching on the actuator, a compressive acoustic wave is generated which rapidly propagates out of the domain (a corresponding expansion wave is observed on switch-off). At the same time, a set of vortices is also generated which lift from the surface of the wing. In the figures, two such structures arising during successive on-events of the actuator have been identified as *A* and *B* respectively. These structures diffuse as they are convected downstream, partly as a consequence of the coarser mesh, but maintain their overall form and can be identified even near the trailing edge. By frame (e), separation inception is apparent near the leading edge, becoming prominent by frame (f). In frames (g) and (h), the actuator is on, injecting momen-

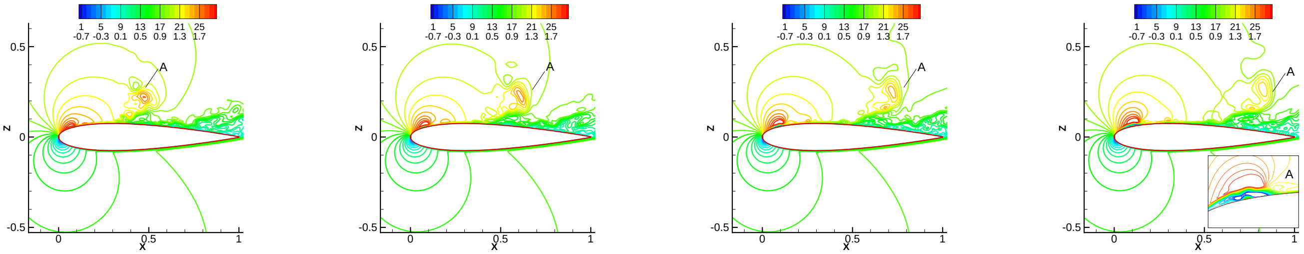

(a) $T = 10.1125T_c$ (b) $T = 10.2125T_c$ (c) $T = 10.3T_c$ (d) $T = 10.3875T_c$

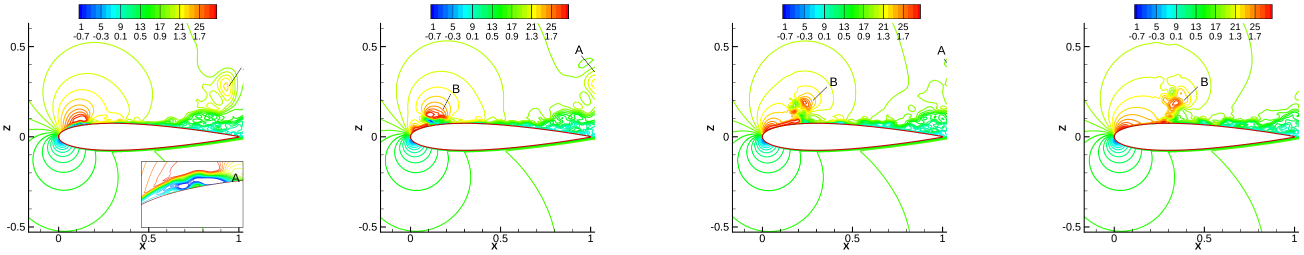

(e) $T = 10.475T_c$ (f) $T = 10.5625T_c$ (g) $T = 10.65T_c$ (h) $T = 10.7375T_c$

Figure 6. ASYMPTOTIC RESPONSE WITH 20% DUTY CYCLE OF INTERPULSE PERIOD OF $0.7T_c$

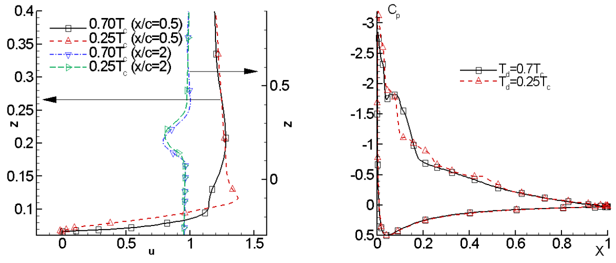

(a) Mean u profiles (b) C_p profiles

Figure 7. EFFECT OF INTERPULSE PERIOD VARIATION ON MEAN RESPONSE

tum near the surface and initiating the formation of new local phenomena preceeded by the vortex pair B, which follows the same development as A, thus repeating the sequence.

The development of incipient separation in the previous simulations suggests that the interpulse period of $0.7T_c$ be reduced. To explore the effect of shorter bursts of more frequent actuation, a simulation was conducted at $T_p = 0.25T_c$. With the same duty cycle and ramp-up and ramp-down times (as a ratio of the duty cycle) the power requirements remain the same. Results after a periodic asymptote is reached have been presented in Ref. [13]. Briefly, reducing the interpulse period results eruption of multiple vortical structures in each cycle. Up to three such structures are observed, with the leading pair being the most distinct. The size of these structures is smaller than in the previous case and, in comparison, their trajectory remains relatively closer to the surface.

Aspects of the time-averaged response to actuation with the two interpulse periods is shown in Fig. 7. Mean velocity profiles are compared at mid-chord and one chord-length downstream of the trailing edge in Fig. 7a. At mid-chord, the shorter interpulse period yields a shallower velocity profile but a sharper and larger peak ($u/U_\infty \sim 1.4$), while the larger period case exhibits a more diffuse distribution. However, these differences are mitigated downstream, where similar velocity defects are observed in the wake. Mean C_p profiles plotted in Fig. 7b indicate that with the exception of the region near the actuator, the mean pressure fields are similar with the two different interpulse periods. Contours of the mean u velocity are presented later, § 5.3 where the various unsteady actuation simulations, both through duty cycles and first-principles simulations, are discussed together.

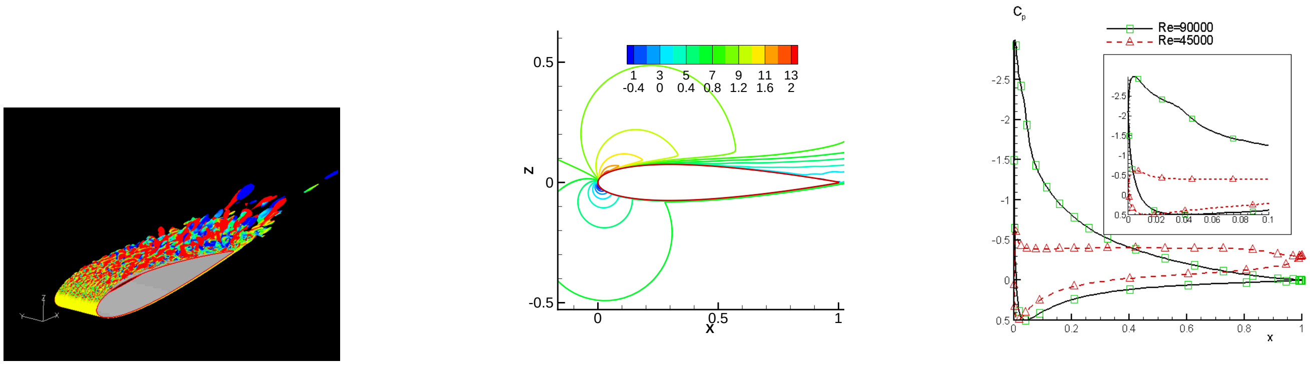

(a) Iso-levels (b) *u*-velocity (c) Surface C_p profiles

Figure 8. EFFECT OF REYNOLDS NUMBER (NO-CONTROL)

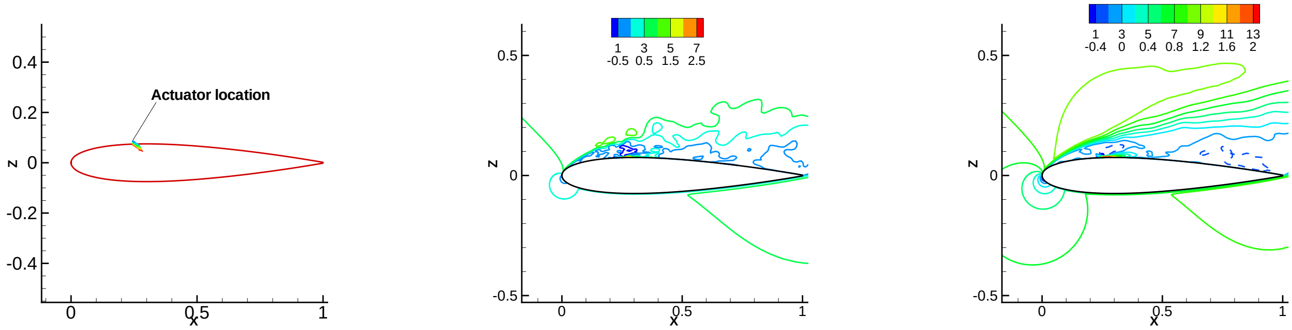

(a) Force location (b) Instantaneous *u* (c) Mean *u*

Figure 9. EFFECT OF ACTUATOR LOCATED AT MAXIMUM THICKNESS LOCATION AT $Re = 90,000$, $\alpha_a = 15^o$

4.4 EFFECT OF REYNOLDS NUMBER AND ACTUATOR LOCATION

When the Reynolds number is increased to $90,000$, the flow becomes turbulent immediately downstream of the leading edge and remains attached in the mean. Figure 8a exhibits instantaneous vorticity magnitude iso-levels colored by magnitude of spanwise vorticity while Fig. 8b displays the mean u velocity at mid-span. The separating shear layer observed previously at lower Reynolds number is absent, and the flow is clearly attached in the mean sense. The surface pressure profile variation, Fig. 8c shows the classic flat shape at the stalled lower Reynolds number case, while the attached flow obtained at higher Reynolds number displays a characteristic suction profile, with a larger suction peak.

Although the flow is attached, two prominent fluid dynamic effects, turbulence and separation, can be coupled to actuator positioning and orientation to yield several different phenomena. In Ref. [12], a "backward"-oriented actuator, *i.e.*, where the actuator is placed so that the embedded electrode is upstream of the exposed electrode and the body force points predominantly against the flow, was shown to induce attachment by triggering turbulence in a separated flow. In a reverse fashion, the "forward" facing actuator may be deployed by suitable placement to laminarize a turbulent flow, and thus induce separation. To demonstrate this, the actuator in the high Reynolds number case is moved from near the leading edge to the point of maximum thickness in the turbulent attached flow, as depicted in Fig. 9a. Instantaneous and mean velocity contours after an asymptotic state is reached, Figs. 9b and c, show that the actuator has triggered separation near the leading edge: in fact, gross manifestations of separation appear shortly after the actuator is turned on. The flow field takes on the character of the no-control lower Reynolds number case in other aspects as well: a trailing edge vortical structure appears that resembles that observed at $Re = 45,000$. These results demonstrate the potential for global actuator impact and highlight the need to consider off-design performance. The dynamics indicate further that inviscid or 2-D simulation procedures are unsuitable for such studies.

Separation can be induced (without control) at the higher Reynolds number by increasing the angle-of-attack to 18^oas observed in instantaneous u-velocity contours of Fig. 10a, which shows separation occurring near mid-chord. The effect of an actuator placed near the leading edge is to generate a laminar attached flow in the impulsive initial transients. However, after several characteristic times, disturbances arising in the shear layer downstream of the trailing edge then move upstream. In the asymptotic state, the flow becomes turbulent near mid-chord, but remains attached in the mean (Fig. 10b).

4.5 ACTUATOR STRENGTH SCALING

Studies on actuator strength effects have also been performed for the two separated flows described above *i.e.,* $Re = 45,000, \alpha = 15^o$ and $Re = 90,000, \alpha = 18^o$ by halving D_c from 2400 to 1200. Results for the latter case are shown in Fig. 11. The instantaneous *u*-velocity contours, Fig. 11a reveal a regular laminar attached flow for a short distance downstream of the actuator near the leading edge. Turbulence sets in at about mid-chord with a rapid growth of the disturbed region. Further, the mean velocity, Fig.11b indicates that the flow remains attached, though the prominence of the wall-jet is clearly diminished when D_c is lowered. Quantitative differences are displayed in the velocity profiles at mid-chord, Fig.11c. The lower forcing yields a wall-jet with a significantly smaller peak velocity, $1.5U_\infty$ versus $2.5U_\infty$ at higher forcing. These results suggest that the effect of turbulence in establishing attachment augments that of the development of a wall-jet. Although not shown, each turbulent attached flow exhibits similar surface C_p profiles. In summary, the above analysis with the *steady* phenomenological model suggest that typically, at lower Reynolds numbers momentum enhancement can yield attachment, while at higher Reynolds numbers, transition to turbulence can yield similar effect. As elucidated below, when the unsteadiness of the force, varying at low radio-frequencies, is taken into account, the latter mechanism is always important beyond the critical Reynolds number. In phenomenological models, similar instabilities may be excited through rapid variations associated with duty cycles, which have the added advantage of reducing power requirement.

5 COUPLING OF FIRST-PRINCIPLES FORCE FIELD

The results of Ref. [12] and those above as summarized from Ref. [13] suggest that manipulation of fluid instabilities provide a powerful lever to enhance actuator effectiveness. Prior simulations have typically employed a duty-cycle approach to generate turbulence, though as noted earlier, steady forces can also be effective if oriented to mimic a sharp adverse pressure gradient. However, there is also an unsteadiness associated with the radio frequency excitation itself (typically $5kHz$) which also has the potential to activate such dynamics even without a duty cycle. A simulation reproducing the unsteadiness of the cycle is therefore essential to distinguish the different mechanisms.

A completely coupled self-consistent solution of both plasma and fluid phenomena, while attractive, is not feasible at this time. The two main reasons are the overwhelming computer resource requirement of 3-D turbulent simulations at plasma time scales as well as gaps in current understanding of the molecular processes that dominate charged particle generation and behavior. For these reasons, in the present work a coupled approach is described to accomplish this objective. Specifically, the force field is obtained from a separate calculation modeling the near-wall flow in a quiescent medium and then scaled and transferred to the wing section. The implicit assumption is therefore that the intermolecular near-wall processes are not sensitive to the outer flow. This requires that the fluid density and pressure, or collisionality, are high, and not much different from those employed in the plasma calculation. This is a reasonable expectation for the low-speed atmospheric pressure incompressible flows of interest here.

5.1 GOVERNING EQUATIONS OF RF FORCE FIELD MODEL

The body force depends on the net space charge and electric field distributions, which are obtained in a self-consistent fashion following the procedure described in Refs. [18–22]. Briefly, the two-dimensional three-species collisional plasma-sheath model includes the charge and momentum continuity equations, and Gauss' law for electric potential:

$$\frac{\partial n_\alpha}{\partial t} + \frac{\partial}{\partial x_j} n_\alpha V_{\alpha j} = n_e z - r n_e n_i \qquad (8)$$

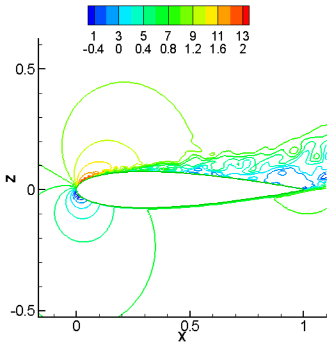

(a) No control

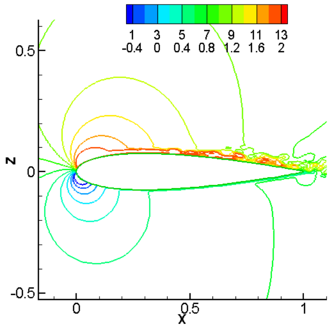

(b) With control, $D_c = 2400$

Figure 10. RESULTS FOR $Re = 90,000, \alpha_a = 18^o$

$$n_\alpha V_{\alpha j} = \text{sgn}(e) n_\alpha \mu_\alpha \frac{\partial \phi}{\partial x_j} - D_\alpha \frac{\partial n_\alpha}{\partial x_j} \tag{9}$$

$$\varepsilon \left(\frac{\partial^2 \phi}{\partial x^2} \right) = e \left(n_e - n_i \right) \tag{10}$$

The charged particle subscript α refers to electrons, e or ions, i respectively, n is the number density, V_j the velocity vector and z and r are the ionization and recombination coefficients. Since air chemistry for the pertinent processes in the discharge remain poorly understood, several assumptions are made to obtain representative features of the time-varying force field. First, the distribution and variation of charge and electric field are obtained under the assumption that the working gas is helium and secondary emission is currently ignored. The scope of this effort is thus on developing the coupling framework and examining fluid response to a force fluctuating at in the $1-10kHz$ frequency range. The effort to lift limitations in current thermo-chemical data for the environment of interest is being pursued separately. A degree of quantitative accuracy is reintroduced through empiricism by scaling the force to match peak amplitudes obtained from the phenomenological considerations of Refs. [9, 11].

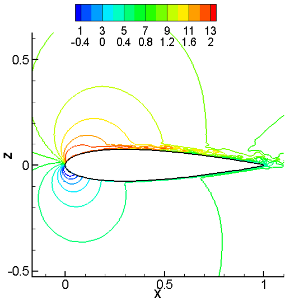

(a) Instantaneous u-velocity, $D_c = 1200$

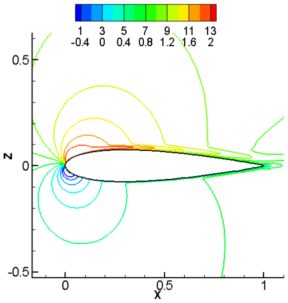

(b) Mean u-velocity, $D_c = 1200$

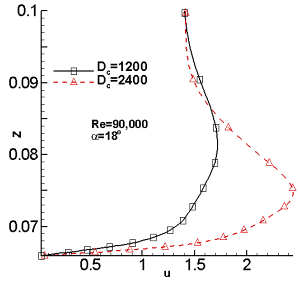

(c) u-profiles at $x = 0.5c$

Figure 11. EFFECT OF ACTUATOR STRENGTH AT ANGLE-OF-ATTACK 18^o AND $Re = 90,000$

The above equations are solved with the multiscale ionized gas (MIG) flow code, developed at the Computational Plasma Dynamics Laboratory at Kettering University. The method is based on a versatile finite-element (FE) procedure adapted from fluid dynamics to overcome the stiffness of the equations generated by multi-species charge separation phenomena. Further details may be found in Refs. [21, 23, 24]. Once the equations are solved, the body force in Eqn. 2 is obtained by noting that $\vec{E} = -\bigtriangledown \phi$ and $\rho_c = n_i - n_e$.

5.2 COUPLING TO 3-D NAVIER-STOKES EQUATIONS

The procedure to transfer forces from the elementary device to the wing section is illustrated in Fig. 12. A small

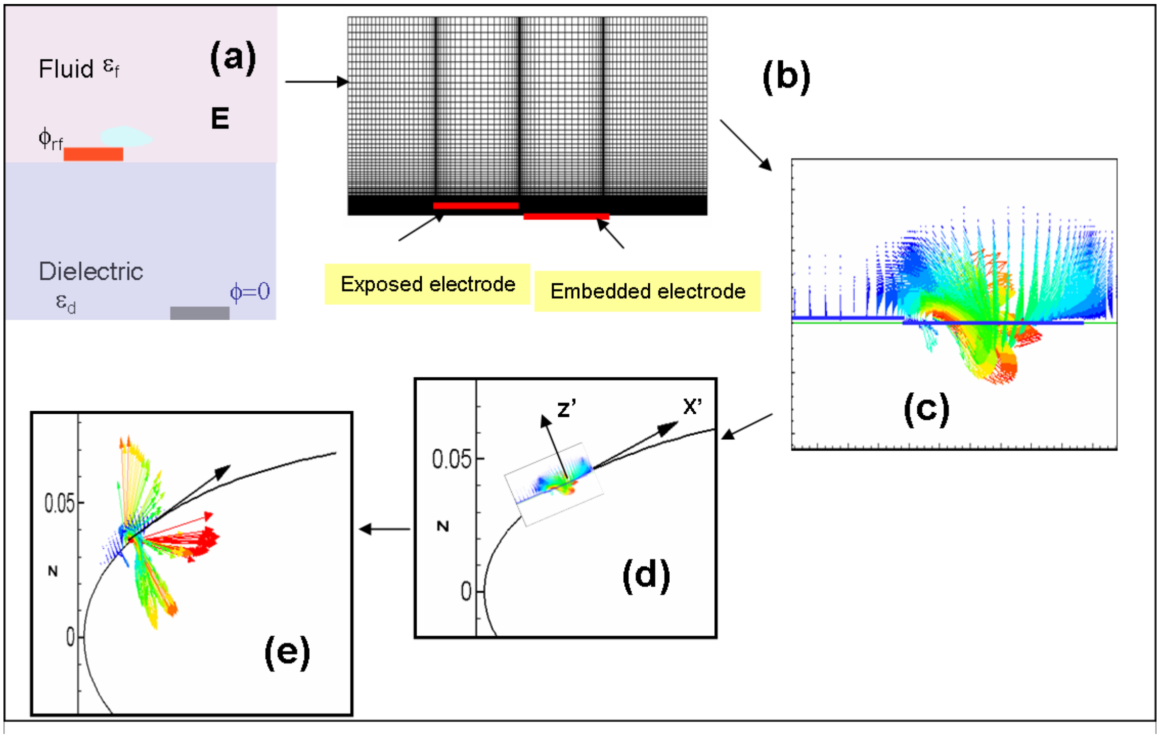

Figure 12. SCHEMATIC OF FORCE TRANSFER PROCEDURE

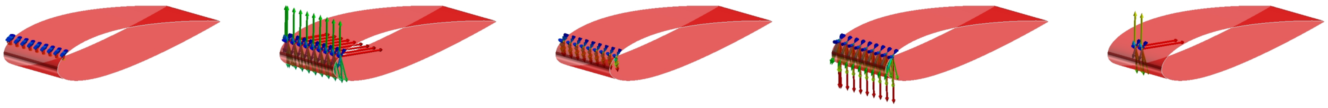

(a) $\phi = 0$ (b) $\phi = \pi/2$ (c) $\phi = \pi$ (d) $\phi = 3\pi/2$ (e) Finite-span forcing

Figure 13. FORCE VARIATION WITH PHASE

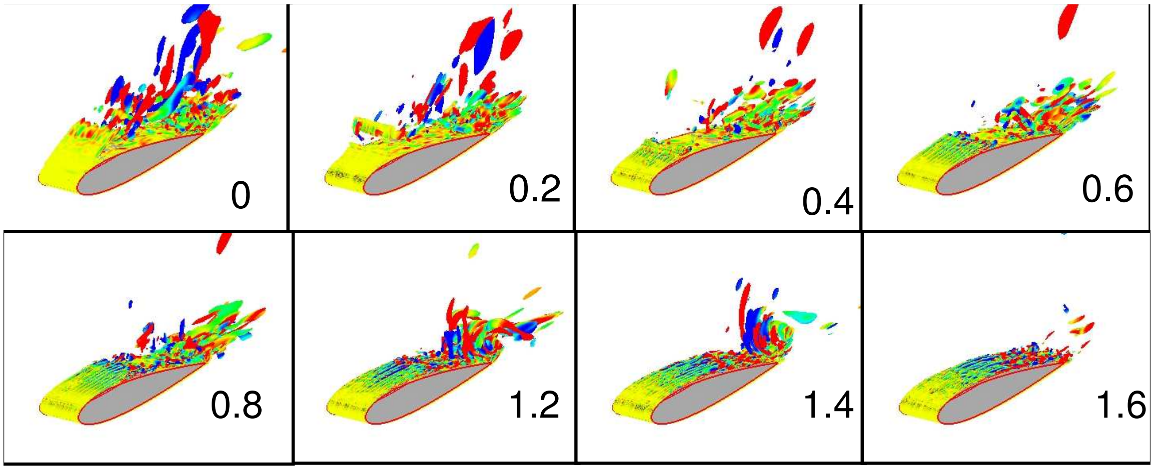

Figure 14. EVOLUTION OF FLOWFIELD WITH $D_c = 2400$

region surrounding the device of Fig. 12a, consisting of two streamwise and vertically staggered electrodes, is discretized with a mesh as shown in Fig. 12b. This region not only includes a judicious area on the side of fluid motion, but also the dielectric region between the two electrodes. The exposed electrode (12*mm* long) is located upstream of the embedded electrode (12.7*mm* long). The vertical distance between the electrodes is 1*mm* and a 0.2*mm* horizontal overlap exists between the two. The exposed electrode is excited at a signal of 5*kHz* and 2*kV rms* amplitude. The dielectric constants of the fluid and solid are assumed to be $1.0055\varepsilon_o$ and $3.5\varepsilon_o$ respectively, where ε_o refers to the property of free space. The mesh employed, shown in Fig. 12b, consists of 103×106 nodes, clustered near the electrodes in the vertical direction, and near electrode edges in the streamwise direction. The vertical height of the simulated domain extends 20*mm* above the surface and 1*mm* beneath it. Inside the dielectric, the only component of current is associated with the change of electric field displacement. At the interface, this value is matched with that associated with electron flow in the fluid towards the surface on which charge accumulation is allowed to occur.

Details of the asymptotic force field obtained on the rectangular region of Fig. 12b may be obtained from Ref. [13]. The pattern at a representative phase angle is shown in Fig. 12c. Since the charge is positive in most regions at this phase angle, the force and electric field are generally similar. The mean force field (not shown) has a predominantly downward/streamwise orientation. In other regions, the force exhibits components away from the surface (over the exposed electrode), as well as towards it (above the dielectric). It has been shown that the average response to the unsteady force bears great resemblance to that obtained with the phenomenological model, though quantitative differences exist for similarly scaled force fields [13], especially near the actuator.

The force field distribution is stored at 20 distinct phases and transferred to the airfoil by first mapping the downstream edge of the exposed electrode to the selected point on the airfoil where the actuator is placed. For the cases described below, this point lies slightly downstream of separation ($X_o = x_o/c = 0.028, Z_o = z_o/c = 0.034$) observed at $Re = 45,000$, $\alpha_a = 15^o$. At this point, a local orthogonal coordinate system, $x' - z'$ is defined such that x' is tangent to the surface. The rectangular domain of Fig. 12c is mapped to this local system by simple rotation operations, Fig. 12d. The domain is scaled by a factor of 100 so that the length and height of the region are roughly 3% and 2% chord respectively, similar to that employed with the phenomenological model [11].

The force contribution is then computed for each point on the wing grid. Care must be taken in performing this task however since the mesh employed for the actuator is much finer than that for the wing. In the simplest approach, each point on the wing is mapped to the scaled and rotated rectangular actuator domain and simple bilinear interpolation is employed. However, this does not take into account the fact that the force at each actuator grid point applies only to the area represented by the grid point. Consequently rapid variations in actuator force are incorrectly accounted for. Another approach is to map each actuator point to a cell on the wing mesh, and to transfer the force to cell corners in inverse proportion to distance. This approach accounts for each point on the finer mesh, but can unrealistically amplify the effect of the larger force magnitude regions, even if they are exerted in limited spatial extent. To address this, area-weighting is employed. Thus the force on each actuator mesh point is multiplied by the area and transferred to the nearest points in the wing mesh. The cumulative force at each wing mesh point is then divided by the area of that point, to ensure that the correct force value is obtained. The amplitude is normalized by peak value in the cycle - this greatly facilitates subsequent magnitude control through the coefficient D_c defined above.

At each time-instant in the Navier-Stokes simulation, the phase angle within a cycle is computed from knowledge of the period of the cycle, and the time at which the control was initiated. It is then a simple matter to linearly interpolate forces between known (stored) adjacent phase angles obtained from the above spatial and temporal integration process. In the cases described below, the non-dimensional time-step was fixed at 5×10^{-5}. Since the non-dimensional period of the 5*kHz* signal is $T_a = 4.7 \times 10^{-3}$, about 95 time-steps span a single cycle.

The force field variation over a cycle is complex - a few select frames have been presented in Fig. 13 a through d. In the "positive" excitation segment, *i.e.,* where the input voltage is positive, the force field very near the surface at X_o, Z_o, is directed downward towards the reference point. Slightly downstream, the force acquires a significant streamwise component as well. Proceeding outwards from the wall, the force obtains an upward-downstream orientation. The amplitudes rise rapidly with time though a small lag is observed between magnitude and phase - the force field is slightly larger in magnitude at $\phi = 6\pi/10$ than at $\phi = 4\pi/10$ while the force field at $\phi = \pi$ is non-zero. On the "negative" stroke, the amplitude of the force is relatively smaller. The force is predominantly towards the surface, though significant upstream components are evident above the embedded electrode. The force is coupled to the wing flow in three different cases. In the first, the value of D_c is the same as in the previous phenomenological results (2400) and extends across the entire span. In the second simulation, D_c is reduced to 240 to examine the growth of instabilities in triggering transition to turbulence. In the last case, the force is again set to $D_c = 2400$ but is applied over a finite span of 0.05*c* in the center of the wing section (see Fig. 13e).

5.3 CONTROL RESULTS WITH FIRST-PRINCIPLES MODEL

In subsequent sections, the unsteady response of the flowfield to the imposed control is first described for all first-principles cases, together with a description of the mean 3-D structure for the finite-span actuator. Subsequently the mean flow is analyzed and compared with results obtained from the duty cyle simulations with the phenomenological model (described earlier in § 4.3).

5.3.1 UNSTEADY RESPONSE TO RADIO-FREQUENCY FORCE FIELD

Figure 14 exhibits the initial response of the flow after the actuator is turned on for $D_c = 2400$ with vorticity iso-levels colored by streamwise vorticity. Actuator operation interrupts the formation of the laminar separated shear layer and the initial structures are convected downstream. Streamwise oriented striations appear near the actuator (see *e.g.,* Fig. 14 at $T = 1.2$). A trailing vortex event, unrelated to control, is evident at $T = 1.2$ and $T = 1.4$. By $T = 1.6$, the initial structures have disappeared and a turbulent flow is observed past mid-chord. The development of the apparent attachment is relatively monotonic, starting near the point of application of the body force and progressing downstream.

Aspects of the instantaneous flow field after an asymptotic state has been reached are shown in Fig. 15. The transitional streamwise oriented structures, Fig. 15a, persist to near the point of maximum thickness, at which point turbulence sets in relatively rapidly. The instantaneous pressure contours, Fig. 15b exhibit the acoustic impact of the actuator, most obvious near the point of application. Although the acoustic signal yields large relative fluctuations compared to the no-control case, their amplitude diminishes with distance, an effect which is enhanced by the coarser mesh resolution away from the surface. The instantaneous *u*-velocity contours, Fig. 15c, show minor fluctuations near the actuator but these are damped relatively rapidly. These results differ significantly from thsoe obtained with the steady force model, where neither the fine scale structures nor the acoustic signal are obtained.

Iso-levels of the initial transients with reduced actuator strength ($D_c = 240$) are shown in Fig. 16. In this case, the striations observed previously do not occur. Rather, the separated shear layer becomes turbulent a short distance downstream of separation, similar to the no-control case. However, the breakdown is more rapid with excitation. Iso-levels of the instantaneous flowfield patterns after asymptotic state is reached, Fig. 17a, show a much larger disturbed region over the wing than at higher forcing. The acoustic signal, Fig. 17b is relatively weaker compared to that obtained with the stronger device. The pressure field contains the signature of the coherence associated with the initial separated shear layer breakdown process. Instantaneous *u*-velocity contours indicate that although the size of the disturbed region has diminished relative to the no-control case, separation persists downstream of the point of maximum thickness.

The flow field obtained with the finite-span actuator ($D_c = 2400$) is described in Fig. 18. Instantaneous iso-levels as before when the asymptotic state is reached are shown in Fig. 18a. The region downstream of the actuator is seen to be characterized by the same longitudenal structures observed for the full span case. However, at the spanwise edges of actuation, instabilities are noted to set in very rapidly. The region of chaotic flow spreads towards the center of the section and after about mid-chord, the flow is turbulent on the entire span. Mean *u*-velocity and vorticity contours at several cross-flow planes are plotted in Figs. 18b and c respectively. The central region near the actuator is characterized by a shallow high-speed jet-like structure of high-vorticity flanked by coherent vortical regions that entrain fluid. Diffusion of these structures is accelerated following the onset of turbulence. The flowfield near the leading edge is consistent with the development of a horse-shoe structure, shown in Fig. 18d with vortex and stream lines. The core of the vortex wraps around the actuator causing a streamwise vortex pair before diffusing due to the onset of turbulence.

5.3.2 MEAN RESPONSE ANALYSIS

With the exception of the finite-span actuator case, all simulations on the wing section are homogeneous in the spanwise direction and the asymptotic mean flow is two-dimensional. In this section, the effect of control is examined on the mean flow obtained with both the unsteady radio-frequency forcing as well as the constant force model modulated with a duty-cycle.

Figure 19 compares the mean flowfield obtained with the baseline flow (Fig. 19a), full-span high forcing (Fig. 19b), full-span low forcing (Fig. 19c), mid-span plane of finite-span forcing (Fig. 19d), and duty cycle simulations shown previously for interpulse periods of $0.7T_c$ (Fig. 19e) and $0.25T_c$ (Fig. 19f). The baseline mean flow exhibits a classic stall pattern, which is eliminated to varying degrees with the different approaches. The high-forcing case is characterized by complete attachment and a relatively thin boundary layer height. When the actuator strength is lowered, although the degree of separation is diminished compared to the stalled situation, it is evident that a significant separated region exists in the latter half of the wing section. The finite-span case (the mean flow at mid-span is shown) also depicts an attached flow. The rate of boundary layer growth near the trailing edge is however higher than in Fig. 19b, suggesting a greater effect of turbulence in the downstream region. The mean flow for both duty cycles is qualitatively similar, though small differences

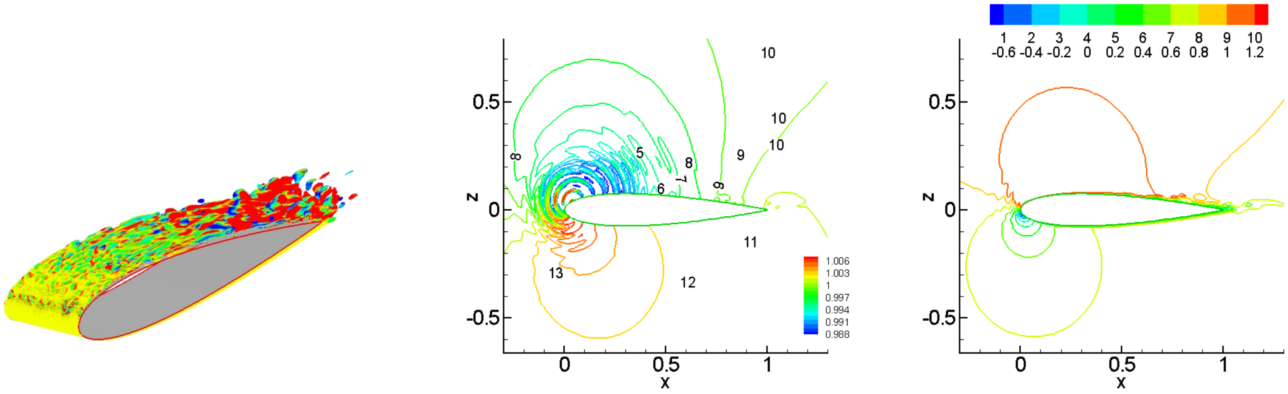

(a) Iso-levels (b) Pressure at mid-span (c) Instantaneous u-velocity

Figure 15. ASPECTS OF INSTANTANEOUS ASYMPTOTIC STATE WITH $D_c = 2400$. NUMBERS ARE TIME AFTER ONSET OF CONTROL.

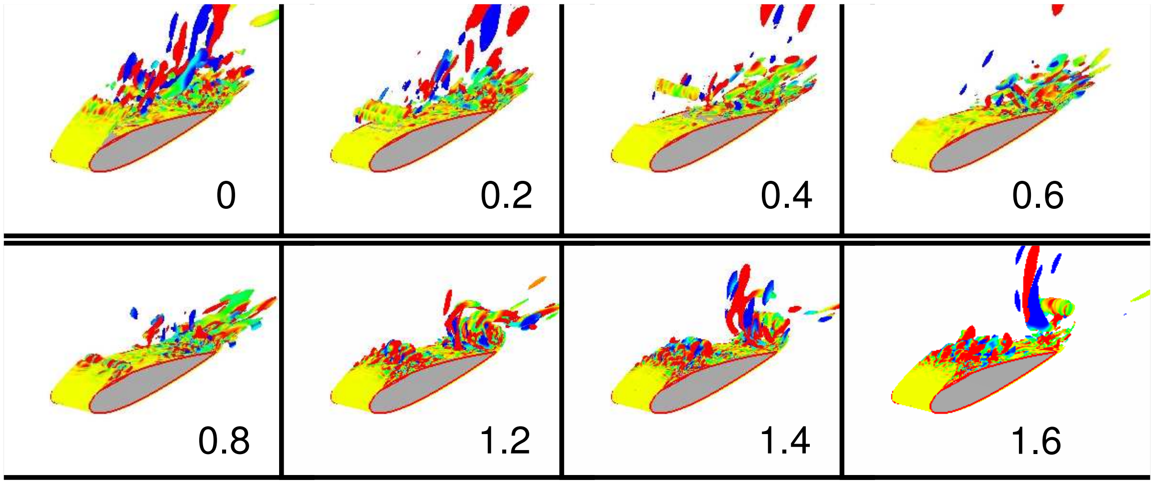

Figure 16. EVOLUTION OF FLOWFIELD WITH $D_c = 240$. NUMBERS ARE TIME AFTER ONSET OF CONTROL.

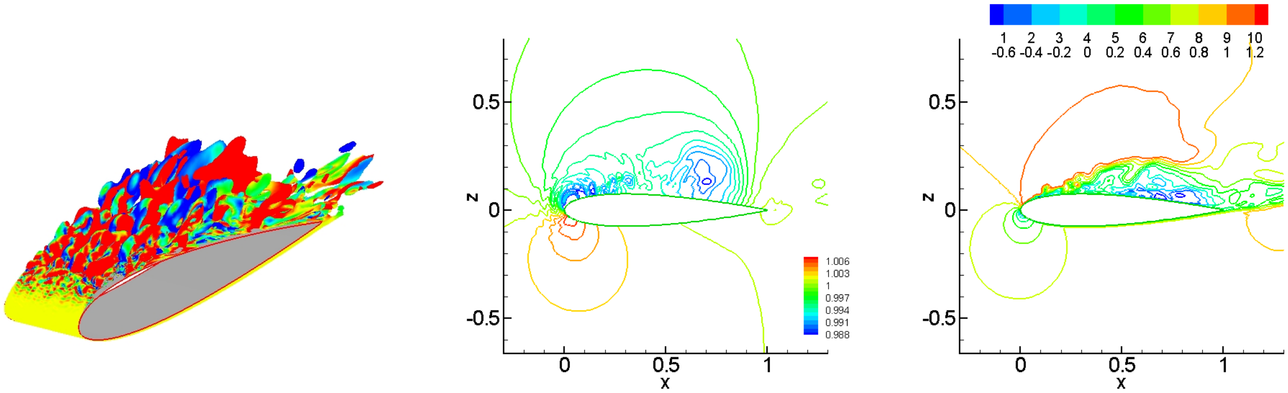

(a) Iso-levels (b) Pressure at mid-span (c) Instantaneous u-velocity

Figure 17. INSTANTANEOUS ASYMPTOTIC STATE WITH $D_c = 240$

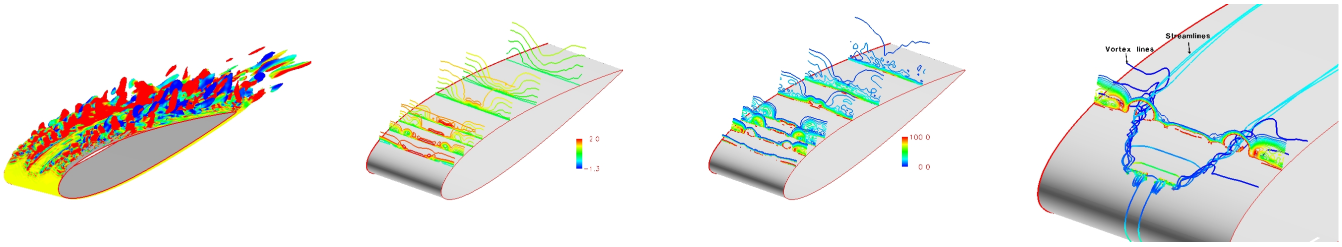

(a) Iso-levels (instantaneous) (b) Mean u-velocity (c) Mean vorticity magnitude (d) Vortex structure in mean fow

Figure 18. ASPECTS OF FLOW WITH FINITE-SPAN ACTUATOR

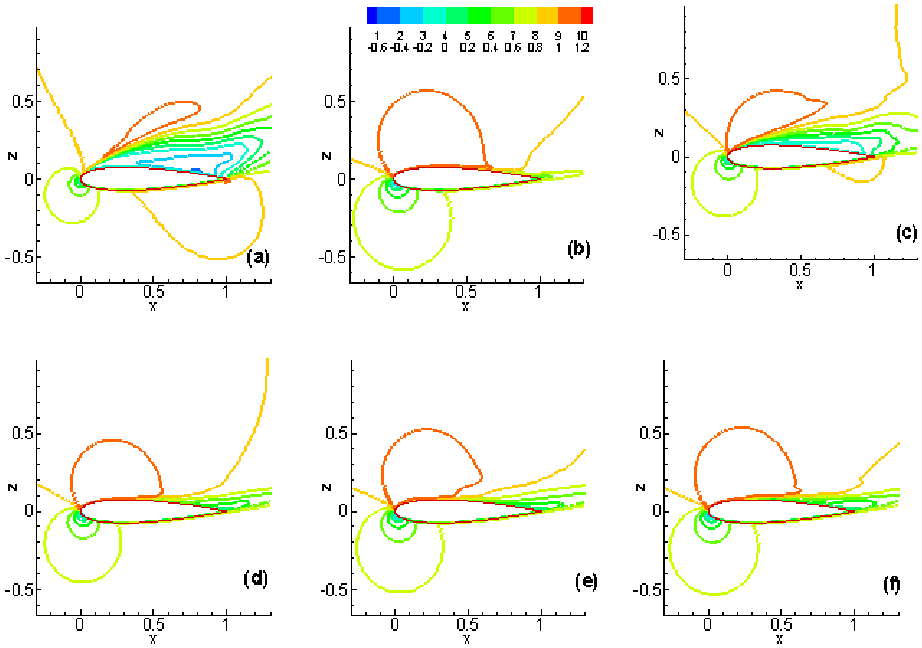

Figure 19. MEAN u-VELOCITY CONTOURS. a: NO-CONTROL, b: $D_c = 2400$, c: $D_c = 240$, d: $D_c = 2400$ (FINITE-SPAN), e: DUTY CYCLE ($T_p = 0.7$), f: DUTY CYCLE ($T_p = 0.25$)

are evident near the trailing edge. Distinctions in the development of the Reynolds stresses are described later.

Figure 20a depicts the velocity profile across the boundary layer at $X = 0.8$ for the different cases. The no-control simulation indicates the expected negative-velocity region extending to about $0.15c$ above the surface. A significant overshoot is observed in the outer flow. Both the high-forcing cases, full-span and finite span, show an attached flow with no reverse flow near the wall. More significantly, in contrast to the steady actuation case shown in Fig. 11, no significant overshoot is evident in either case indicating the absence of a mean wall-jet. The finite-span case further indicates a larger boundary layer, suggesting a wider impact of the turbulence mechanism than with full-span forcing. For the low forcing case, separation is evidently not eliminated, but the size of the reversed flow region is clearly smaller than without control and the overshoot in velocity is reduced. Turning to the duty-cycle simulations, neither indicates mean separation and only the smaller period case shows a very small overshoot near the edge of the boundary layer. A comparison of mean C_p profiles for each case is shown in Fig. 20. The effect of control is to increase suction to varying extent, while there is relatively little qualitative effect on the lower surface variation. The most effective approaches are the duty cycle methods, as well as the higher forcing unsteady force methods. The low forcing value also yields a gain consistent with the reduction in separation, but it is smaller than the other approaches. All control techniques increase the pressure at the trailing edge.

A description of the impact of actuation on turbulence is provided in the context of the main Reynolds stress com-

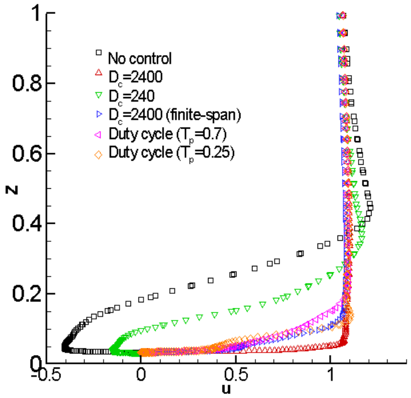

(a) u-velocity at $X = 0.8$

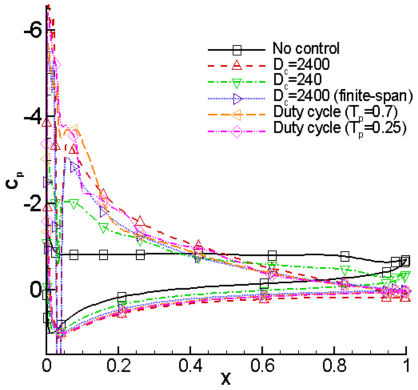

(b) C_p

Figure 20. COMPARISON OF MEAN PROFILES FOR VARIOUS CONTROL TECHNIQUES

ponents which are depicted in Figs. 21, 22 and 23 for the various cases. The normal stresses depict the largest values, and each is modulated to varying extent with the various forms of control. Of particular interest however are the cross-correlations shown in Fig. 22 representing transverse momentum transfer typically associated with separation control. For the uncontrolled case, these stresses occur in the shear layer and separated region above the wing section. Positive values are observed both in the separation and trailing edge shear layers while the dominant component above the wing section is negative. When control is applied, positive correlations appear near the actuator application region, while the boundary layer developing downstream exhibits negative values. Comparison of full (Fig. 22b) and finite-span (Fig. 22c) actuation shows that the latter induces higher turbulence levels than the former. This observation is compatible with the previously noted development of horseshoe vortices which have the effect of destabilizing the flow. The low forcing case (Fig. 22c) is also successful at influencing the turbulence structure of the flow. In this case, the negative correlated regions are drawn towards the surface. The higher frequency duty cycle ($T_p = 0.25$, Fig. 22f) shows greater turbulence stress than the lower frequency case (Fig. 22e). This is consistent with previous observation in § 4.3, that increasing the frequency of the duty cycle has the effect of restraining the ejected vortical structures nearer the wall. A further comparison of results with monochromatic radio-frequency forcing (Fig. 22b) and duty cycle variation of a steady force (Fig. 22f) at the same D_c is illustrative. It is evident that the turbulence levels in the latter calculation are higher than in the former, even though the power level is smaller because the actuator is on for only 20% of the time. This suggests that wide-spectrum input provided by the rapid on/off phases during the duty cycle are a more effective mechanism for turbulence amplification, and thus separation control. These results are consistent with the comprehensive results of Ref. 25, where various unsteady excitation mechanisms are discussed.

6 CONCLUSION

The effectiveness of radio-frequency based plasma actuators, operating under the mechanics of dielectric barrier discharges, to reduce or eliminate stall on airfoils at high angles of attack has been explored. Phenomenological models, both steady and encapsulated into a duty cycle variation, as well as unsteady force fields from first-principles radio-frequency excitation have been studied. Parameters varied include Reynolds number, angle of attack, duty cycle frequency and actuator strength and location. The results show that the flow structure obtained with a force varying at radio-frequencies ($5kHz$) is significantly different in detail from that obtained with a steady actuator. By exciting instabilities in the separated shear layer, fine scale features arise through transition to turbulence, which are absent in steady actuation. Other mechanisms to trigger or enhance turbulence include duty cycles, which have the added advantages of multi-frequency input and reduced power requirement, and finite-span actuation, which generates coherent structures near the device to accomplish similar destabilizing effects. Further work is required to extend the the present analysis, which considers monochromatic radio-frequency signals, to wide-frequency excitation associated with more complex waveforms.

ACKNOWLEDGMENTS

The authors are grateful for support from the Air Force Office of Scientific Research, under tasks monitored by Dr. J. Schmisseur and Dr. F. Fahroo. This work was also sponsored in part by a grant of computer time from the Department of Defense High Performance Computing Shared Resource Centers at the Army High Performance Computing Research Center (AHPCRC), Naval Oceanographic Office (NAVO), Aeronautical Sciences Center (ASC) and the Engineer Research and Development Center (ERDC).

REFERENCES

[1] Roth, J., Sin, H., R.C.M., M., and Wilkinson, S., 2003. "Flow re-attachment and acceleration by paraelectric and peristaltic electrohydrodynamic effects". *AIAA Paper 2003-531*, Jan.

[2] Post, M., and Corke, T., 2003. "Separation control on high angle of attack airfoil using plasma actuators". *AIAA Paper 2003-1024*.

[3] Post, M., and Corke, T., 2004. "Separation control using plasma actuators - dynamic stall control on an oscillating airfoil". *AIAA Paper 2004-2517*, June.

[4] Opaits, D., Roupassov, D., Starikovskaia, S., Starikovskii, A., Zavialov, I., and Saddoughi, S., 2005. "Plasma control of boundary layer using low-temperature non-equilibrium plasma of gas discharge". *AIAA Paper 2005-1180*, Jan.

[5] Jacob, J., Rivir, R., Carter, C., and Estevadeordal, J., 2004. "Boundary layer flow control using ac discharge plasma actuators". *AIAA Paper 2004-2128*, June.

[6] Jacob, J., Ramakumar, K., Anthony, R., and Rivir, R., 2005. "Control of laminar and turbulent shear flows using plasma actuators". *Fourth Int. Symp on Turbulence and Shear Flow Phenomena*(TSFP4-225), June.

[7] Hultgren, L., and Ashpis, D., 2003. "Demonstration of separation delay with glow-discharge plasma actuators". *AIAA Paper 2003-1025*.

[8] Roth, J., 2003. "Aerodynamic flow acceleration using paraelectric and peristaltic electrohydrodynamic (ehd) effects of a one atmosphere uniform glow discharge plasma (oaugdp)". *Phys. Plasmas*, **10**, p. 2117.

[9] Shyy, W., Jayaraman, B., and Andersson, A., 2002. "Modeling of glow-discharge induced fluid dynamics". *J. Appl. Phys.*, **92**, p. 6434.

[10] Baird, C., Enloe, C., McLaughlin, T., and Baughn, J., 2005. "Acoustic testing of the dielectric barrier discharge (dbd) plasma actuator". *AIAA Paper 2005-0565*, Jan.

[11] Gaitonde, D., Visbal, M., and Roy, S., 2005. "Control of flow past a wing section with plasma-based body forces". *AIAA Paper 2005-5302*.

[12] Visbal, M., and Gaitonde, D., 2006. "Control of vortical flows using simulated plasma actuators". *AIAA Paper 2006-0505*.

[13] Gaitonde, D., Visbal, M., and Roy, S., 2006. "A coupled approach for plasma-based flow control simulations of wing sections". *AIAA Paper 2006-1205*.

[14] Visbal, M., and Gaitonde, D., 1999. "High-Order Accurate Methods for Complex Unsteady Subsonic Flows". *AIAA Journal*, **37**(10), pp. 1231–1239.

[15] Gaitonde, D., Shang, J., and Young, J., 1999. "Practical Aspects of Higher-Order Numerical Schemes for Wave Propagation Phenomena". *Int. Jnl. for Num. Methods in Eng.*, **45**, pp. 1849–1869.

[16] Gaitonde, D., and Visbal, M., 2000. "Pade-type higher-order boundary filters for the navier-stokes equations". *AIAA J.*, **38**(11), Nov., pp. 2103–2112.

[17] Corke, T., and Post, M., 2005. "Overview of plasma flow control: Concepts, optimization and applications". *AIAA Paper 2005-0563*.

[18] Roy, S., and Gaitonde, D., 2004. "Radio frequency induced ionized collisional flow model for application at atmospheric pressures". *J. Appl Phys*, **96**, pp. 2476–2481.

[19] Roy, S., and Gaitonde, D., 2005. "Multidimensional collisional dielectric barrier discharge for flow control at atmospheric pressures". *AIAA Paper 2005-4631*.

[20] Roy, S., 2005. "Flow actuation using radio frequency in partially-ionized collisional plasmas". *Appl. Phys. Letters*, **86**(101502:1-3).

[21] Roy, S., Singh, K., Kumar, H., Gaitonde, D., and Visbal, M., 2006. "Effective discharge dynamics for plasma flow control". *AIAA Paper 2006-0374*, Jan.

[22] Roy, S., Singh, K., and Gaitonde, D., 2006. "Dielectric barrier plasma dynamics for active control of separated flows". *Appl. Phys. Letters*, **88 (121501)**(12).

[23] Balagangadhar, D., and Roy, S., 2001. "Design sensitivity analysis and optimization of steady fluid-thermal systems". *Computer Methods in Applied Mechanics and Engineering*, **190**, Aug., pp. 5465–5479.

[24] Roy, S., and Pandey, B., 2003. "Development of a finite element-based hall-thruster model". *J. Prop. Power*, **19**, pp. 964–975.

[25] Visbal, M., Gaitonde, D., and Roy, S., 2006. "Control of transitional and turbulent flows using plasma-based actuators". *AIAA Paper 2006-3230*, June.

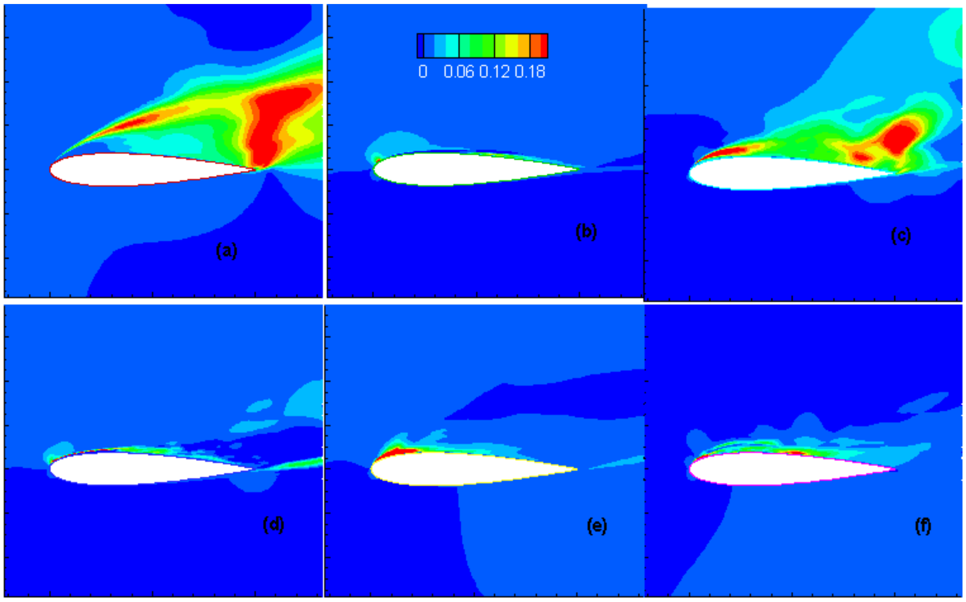

Figure 21. COMPARISON OF $< uu >$ REYNOLDS STRESSES. a: NO-CONTROL, b: $D_c = 2400$, c: $D_c = 240$, d: $D_c = 2400$ (FINITE-SPAN), e: DUTY CYCLE ($T_p = 0.7$), f: DUTY CYCLE ($T_p = 0.25$)

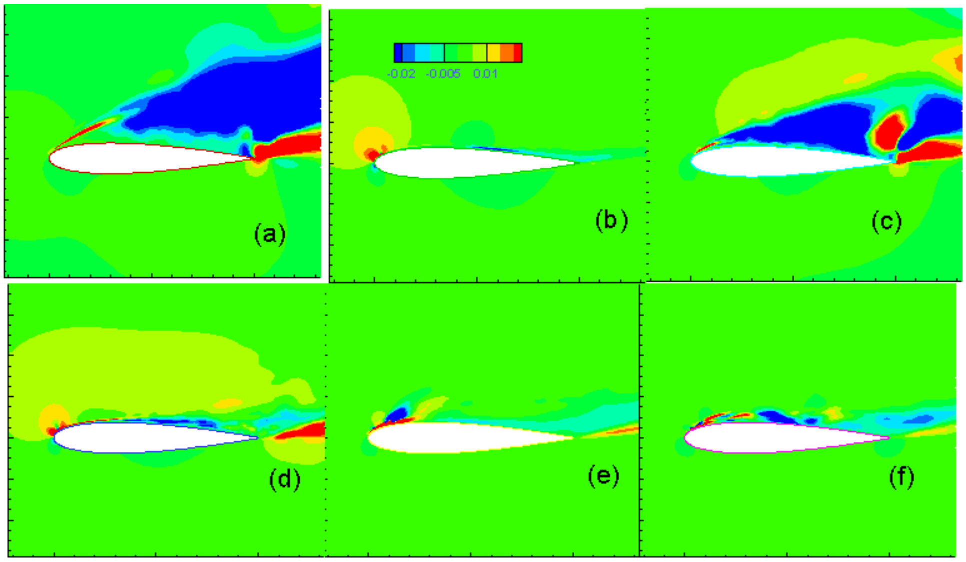

Figure 22. COMPARISON OF $< uw >$ REYNOLDS STRESSES. a: NO-CONTROL, b: $D_c = 2400$, c: $D_c = 240$, d: $D_c = 2400$ (FINITE-SPAN), e: DUTY CYCLE ($T_p = 0.7$), f: DUTY CYCLE ($T_p = 0.25$)

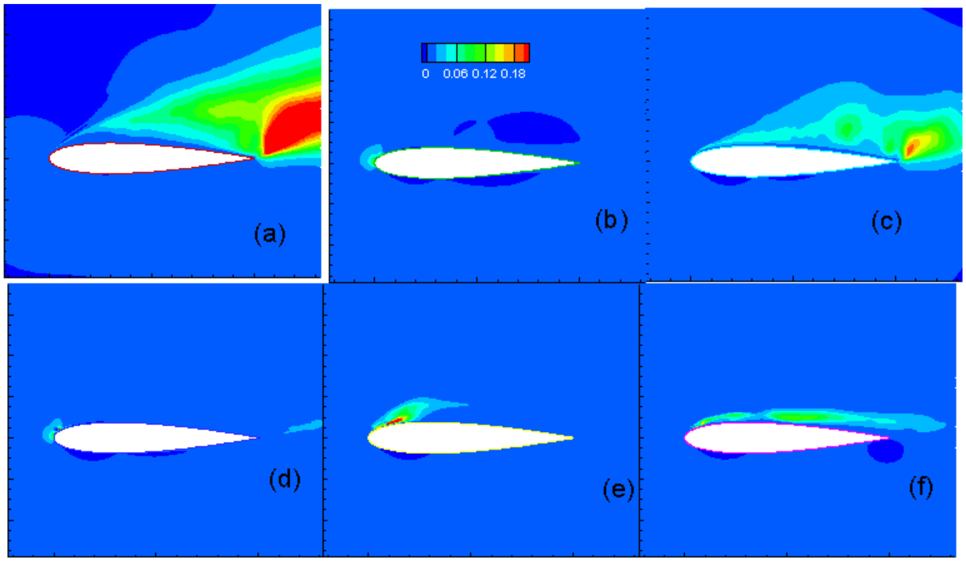

Figure 23. COMPARISON OF $< ww >$ REYNOLDS STRESSES. a: NO-CONTROL, b: $D_c = 2400$, c: $D_c = 240$, d: $D_c = 2400$ (finite-span), e: DUTY CYCLE ($T_p = 0.7$), f: DUTY CYCLE ($T_p = 0.25$)